This is a preprint, the final version is subject to change, of the American Mineralogist (MSA)
Cite as Authors (Year) Title. American Mineralogist, in press.
(DOI will not work until issue is live.) DOI: http://dx.doi.org/10.2138/am-2017-6089

Subsolidus hydrogen partitioning between nominally anhydrous minerals in garnet-bearing peridotite

Sylvie Demouchy[1]*, Svyatoslav Shcheka[2], Carole M.M. Denis[1], Catherine Thoraval[1]

[1]Géosciences Montpellier, Université Montpellier & CNRS, Montpellier, France

[2]Bayerisches Geoinstitut, Universität Bayreuth, Bayreuth, Germany

#6089, Revision 2 for American Mineralogist

April 2017

* corresponding author: demouchy@um2.fr

Phone (office): +33 4 67 14 49 42

Phone: (lab) +33 4 67 14 36 03

Fax: +33 4 67 14 36 03

Abstract

Hydrogen distribution between nominally anhydrous minerals (NAMs) of a garnet-lherzolite under subsolidus conditions has been investigated. Separated NAMs from a garnet-peridotite from Patagonia (Chile) are annealed together (olivine, orthopyroxene, clinopyroxene and garnet) using a piston-cylinder at 3 GPa and 1100 °C using talc-Pyrex cell assembly for 10, 25 and 100 hours. The talc-pyrex assembly provides enough hydrogen in the system to re-equilibrate the hydrogen concentrations at high pressure. The three co-existing nominally anhydrous minerals (NAMs, i.e., olivine, orthopyroxene and clinopyroxene) were successfully analyzed using FTIR. The resulting hydrogen concentrations exceed significantly the initial hydrogen concentration by a factor of 13 for olivine and a factor of 3 for both pyroxenes. Once mineral-specific infrared calibrations are applied, the average concentrations in NAMs are 115±12 ppm wt H_2O for olivine, 635±75 ppm wt H_2O for orthopyroxene and 1214±137 ppm wt H_2O for clinopyroxene, garnet grains are dry. Since local equilibrium seems achieved over time (for 100 hours), the calculated concentration ratios are interpreted as mineral-to-mineral hydrogen partition coefficients (i.e., Nernst ‘s law) for a garnet-peridotite assemblage. It yields, based on mineral-specific infrared calibrations, Dopx/ol=5±1, Dcpx/ol= 10±2, and Dcpx/opx=1.9±0.4. While Dcpx/opx is in agreement (within error) with previous results from experimental studies and concentration ratios observed in mantle-derived peridotites, the Dpx/ol from this study are significantly lower than the values reported from mantle-derived xenoliths and also at odd with several previous experimental studies where melt and/or hydrous minerals co-exists with NAMs. The results confirm the sensitivity of hydrogen incorporation in olivine regarding the amount of water-derived species (H) in the system and/or the amount of water in the co-existing silicate melt. The results are in agreement with an important but incomplete dehydration of mantle-derived olivine occurring at depth, during transport by the host magma or during slow lava flow cooling at the surface. The rapid concentration modification in mantle pyroxenes also points out that pyroxenes might not be a hydrogen recorder as reliable as previously thought.

Key words: olivine, pyroxenes, hydrogen, partition coefficient, upper mantle.

Highlights

- H partitioning coefficients between NAMs are quantified at 3 GPa and 1100°C
- Subsolidus partitioning differs from experiments with co-existing silicate melt
- Subsolidus bulk H content at 3 GPa (100 km) is estimated to ~ 340 ppm wt H_2O

Introduction

The distribution of hydrogen among the mantle minerals remains a key parameter to assess the contribution of the deep planet reservoir to the Earth's water cycle. Indeed several physical and chemical properties of the mantle minerals and rocks are sensitive to the amount of water (i.e., molecular water and water-derived species, such as hydroxyl, hydrogen and protons) present in the geological system. One can mention melting temperature (e.g., Gaetani and Grove, 1998), electrical conductivity (e.g., Karato, 1990; Yoshino, et al., 2006), seismic wave velocities (e.g, Inoue et al., 1998; Jacobsen et al., 2004; Jacobsen, 2006), ionic diffusion (e.g., Hier-Majunder et al., 2004; Costa and Chakraborthy, 2008; Demouchy et al., 2007; Gasc et al., 2016) and possibly viscoplastic deformation (Mackwell et al., 1985; Kohlstedt, 2006; Demouchy et al., 2012; Tasaka et al., 2016). These deep processes are all crucial players in geodynamics. To date, two approaches are currently used to quantify hydrogen in mantle nominally anhydrous minerals (NAMs): (1) measurements on natural samples such as mantle-derived xenoliths and peridotites from exhumed massifs or (2) experimental petrology and mineralogy. The first approach focuses on natural observations. Nevertheless, it only allows for a partial comprehension and quantification since many mantle processes are combined and in competition with each other (e.g., partial melting, various successive types of metasomatism, metamorphism, exhumation and surface weathering, see Bell and Rossmann, 1992; Dobson et al., 1995; Grant et al., 2007). The second approach has been hitherto very successful and provided a large amount of data for a wide range of pressures, temperatures, water or oxygen fugacities or chemical systems (e.g., Sweeney et al., 1997; Bolfan-Casanova et al., 2000; Asimow, 2001; Koga et al., 2003; Aubaud et al., 2004; 2008; Hauri et al. 2006; Mosenfelder et al., 2006; Bali et al., 2008; Tenner et al., 2009; Withers et al., 2008, 2011; Férot and Bolfan-Casanova, 2012; Ardia et al., 2012; Kovács et al.,

96 Novella et al., 2014; Gaetani et al., 2014; Sokol et al., 2013, 2014; Green et al., 2014; Yang et al.,
97 2015; see also Hirschmann, 2005 and Hirschmann et al., 2009 for reviews). However, these past
98 experimental studies have focused on melt genesis and thus the hydrogen partition coefficients
99 are obtained for systems where the NAMs are always co-existing with a large amount of hydrous
100 melt (quenched as glass with/without quenched crystals). Since this type of experiments and
101 subsequent chemical measurements are particularly difficult, a full set of inter-mineral hydrogen
102 partition coefficients are rarely calculated from a single experiment but rather derived from a
103 batch of experiments containing hydrous melt and at least one NAM.

104 For subsolidus conditions, as along a standard geotherm, the lack of partition coefficient
105 is striking (only one study: Kovács et al., 2012, NAMs with co-existing amphibole +/- melt). The
106 inter-mineral partition coefficients are required when calculating (1) the bulk hydrogen
107 concentration when only one mineral is analyzed and (2) the effect of hydrogen on physical and
108 chemical properties, for melt-free peridotites. Ideally, both approaches, quantification of water in
109 natural specimens and experimental mineralogy, should be combined to provide the hydrogen
110 concentration in each mantle mineral at depth.

111 Here, we have performed high pressure, high temperature annealing experiments under
112 hydrogenation conditions below the solidus temperature of garnet-bearing peridotites. Indeed, the
113 melting temperature is around 1500°C for dry peridotite, and around 1010 °C for H_2O-saturated
114 peridotite, according to the seminal study by Hirth and Kohlstedt (1996). For the bulk water
115 content addressed here, and according to the recent study by Katz et al., (2003), which provides
116 melting curves in water-poor conditions, the experimental conditions are sub-solidus. For water-
117 rich systems, see also Grove et al., (2006); Hirschmann (2010) and Green et al., (2014). For the
118 first time, hydrogen incorporation is achieved by ionic diffusion of protons from the high

pressure assembly. Finally, consequences for NAMs as recorders of hydrogen concentrations are discussed.

Method

Sample description and preparation

The samples used for the high pressure experiments are nominally anhydrous minerals (NAMs) which are hand-picked from a garnet-bearing peridotite from Pali-Aike (Chile). The peridotite was previously studied by Stern et al., (1999); Demouchy, (2004) and Demouchy et al., (2006). It is a lherzolitic xenolith, composed of millimetric olivine, enstatite (opx), diopside (cpx) and garnet, which has reached equilibrium in major elements composition (Stern et al., 1999). The equilibrium temperature has been estimated to 1050±50 °C (i.e., Ca-in-opx from Brey and Köhler, 1990) and equilibrium pressure to 2.2-2.4 GPa. Major elements compositions are available elsewhere (Demouchy, 2004) and are reproduced here as convenience in the supplementary material (Table S1). The dehydration concentration profiles, which were interpreted as the results of ionic diffusion, were observed in olivine but not in pyroxenes (Demouchy, 2004; Demouchy et al., 2006), suggesting a fast remobilization of H in olivine and caught-in-the-act by a rapid magma ascent towards the surface. In this study, optically clear and crystallographically not oriented crystals were selected; olivine and opx grains were hand-polished on both sides. Cpx and garnet were not polished and were added to the starting material (or starting mixture).

High pressure experiments

All the experiments reported here were performed at Bayerishes Geoinstitut (Germany). High pressure assemblies were prepared by placing several doubly hand-polished submillimetric size crystals of iron-bearing olivine and opx, with submilimetric grains of cpx and garnet inside a $Pt_{0.95}Rh_{0.05}$ half-welded capsule (0.25 mm wall thickness). At least 10 grains of olivine and opx (medium to large grains), 5 to 14 grains of clinopyroxene and 2 to 4 grains of garnet are piled up on each other inside the capsule. The half-welded capsules were lined up with Ni foil (0.14 mm of thickness) and a minute amount of NiO was added at the bottom of the capsule to buffer oxygen fugacity along Ni-NiO joint (McCammon, 2005; Frost and McCammon, 2008). Each half-welded capsule was also lined with Au foil (0.18 mm) to minimize horizontal cracks during thermal quench and decompression. Fine powder of olivine+10%opx was packed around and above the crystal pile up. A $Pt_{0.95}Rh_{0.05}$ lid was finally placed at the capsule top and micro-arc welded. The mineral mode of the original peridotite was not strictly respected. Here, ol, opx and cpx grains ($\simeq$ 0.04 g, respectively) were used in equal amount to increase probability to successfully analyze pyroxenes later on by Fourier transform infrared spectroscopy (FTIR). Nevertheless, taking into account the amount of olivine+10%opx powder and the amount of ol, opx and cpx grains, it yields a relative weight proportion of 68%, 19%, 12% and 2% for ol, opx, cpx and garnet respectively. The mineral distribution is then in agreement with mineral modes reported for mantle-derived peridotites (e.g., see Demouchy and Bolfan-Casanova, 2016, for a compilation). It yields a bulk content of $\simeq$ 0.009 H_2O wt.% (from 86 to 136 ppm wt H_2O).

According to Katz et al., (2003), which provides water-poor melting curves, the experimental conditions are thus sub-solidus. Neither free distilled water, nor brucite nor talc is added inside the capsule. Typical capsule set up is shown in Figure 1. The capsules were then placed in 1/3-inch talc cell for piston-cylinders. Experiments were performed in an end-loaded piston-cylinder apparatus. A friction correction of 5% was applied to correct the nominal pressure based

experimental data on the quartz–coesite transition at 790 °C (see Bose and Ganguly, 1995 for details). Temperature was controlled using a Pt-$Pt_{90}Rh_{10}$ thermocouple (S-type) with an estimated uncertainty of ±10 °C (Li et al., 2013). Three runs at 3 GPa were annealed at 1100 °C for durations of 10, 35 and 100 hours. Flux of H from the talc cell outside the capsule during the run provided enough protons (H) to enable hydration. Since annealing duration under hydrous conditions over 10 h at temperature above 900 °C is long enough to reach hydrogen saturation at pressures above 0.2 GPa in olivine (Demouchy and Mackwell, 2006) and in pyroxenes as well (Stalder and Skogby 2003; Stalder and Behrens 2006; Ferris et al., 2015; 2016), we expected similar kinetics of H diffusion in this new set up. Note that H diffusion through metal is faster than in silicates with diffusivities around 10^{-8} m^2s^{-1} at 800 °C in nickel (e.g., Wimmer et al., 2008) or $10^{-8}m^2s^{-1}$at 500 °C in platinum (Cermàk et al., 1979). Temperature quench rate was 80-120 °C/s. Pressure release was performed over 12 hours in attempt to reduce post-quench fracturing. Experimental conditions are summarized in Table 1.

Fourier transform infrared spectroscopy

Each capsule was hand double-polished for unpolarized and polarized FTIR analyses. The capsule sections were cleaned several times in a pure acetone bath for at least 12 h to dissolve intergranular Crystal Bond glue. FTIR spectroscopy analyses were performed at the Laboratoire Charles Coulomb at University of Montpellier (France) using a Bruker IFS66v coupled with a Hyperion 3000 Bruker microscope and a liquid nitrogen-cooled mercury-cadmium-telluride (MCT) detector. A Globar light source and a Ge-KBr beam splitter were used to generate Mid Infrared Light (MIR). A wire-gird polarizer on Zn-Se substrate was used to generate polarized IR

radiation. A background measurement was performed before each analysis. Measurements were acquired with a square aperture yielding a square beam spot between 50 and 100 µm. More than two hundred scans were accumulated with a resolution of 4 cm^{-1} for each measurement. A baseline correction was applied on each spectrum using the OPUS software. Fractures were strictly avoided. The sample thickness was measured using a micrometer with an accuracy of ± 1 µm and range from 204 to 368 µm. Spectra were normalized to a thickness of 1 cm. Unfortunately, IR profiles across the large crystal could not be acquired after annealing at high pressure, due to cracks and lack of sharp grain edges.

Several calibrations can be used to quantify the hydrogen concentration. The frequency-dependent calibration of Paterson (1982) was used to quantify the concentration of OH in NAMs as follows:

$$C_{OH} = \frac{X_i}{150\zeta} \int \frac{k(\bar{\nu})}{(3780 - \bar{\nu})} d\bar{\nu} \qquad \text{eq. 1}$$

where C_{OH} is the hydroxyl concentration (in mol H/l), ζ is an orientation factor (=1⁄3 for unpolarized measurements or =1 on for polarized measurements, Paterson, 1982), and $k(\nu)$ is the absorption coefficient in cm^{-1} for a given wavenumber ν. *Xi* is a density factor equal to 2695 ppm H_2O wt, for iron-bearing olivine, 2727 ppm H_2O wt, for mantle enstatite, 2769 ppm H_2O wt, for Cr-diopside, and 2408 ppm H_2O wt, for mantle-derived garnet (for details on the calculation method, see Bolfan-Casanova et al. 2000; Demouchy and Bolfan-Casanova, 2016). For the given thickness of the polished crystals (Table 1), the detection limit of FTIR spectroscopy is 1 to 3 ppm H_2O wt, and uncertainty on the hydrogen concentration is 15% to 30 % (e.g., Demouchy and Mackwell 2003). The calibration of Paterson applied on unpolarized spectra has been recurrently

214 considered to underestimate the hydrogen content (e.g., Withers et al., 2012). Nevertheless, the
215 frequency–dependent calibration of Paterson enables to use the same method to extract hydrogen
216 concentration from the different NAMs. However, in an attempt to improve accuracy on
217 hydrogen concentration in all NAMs, we also used mineral-dependent calibrations (i.e., Bell et
218 al., (1995) for pyroxenes and Withers et al. (2012) for iron-bearing olivine), which required the
219 use of polarized IR light (see compilation of methods in Demouchy and Bolfan-Casanova, 2016).
220 Unfortunately, the natural minerals used in the experiments were not crystallographically
221 oriented and we have counteracted this problem by averaging numerous polarized FTIR spectra
222 (as proposed by Asimow et al., 2006), taken at various orientations (rotation step of 45° of the
223 polarizer respective to the sample position), to calculate an average polarized spectrum before
224 applying the mineral-dependent calibrations (see Withers et al., 2012; Demouchy and Bolfan-
225 Casanova, 2016).

226 Once the unpolarized and polarized spectra for each phase and for each experiment were
227 at hand, there was no significant differences between them (Fig. S1, which confirms the studies
228 by Kovács et al., 2008; Shuai and Yang, 2017). We have hence chosen to average all spectra
229 together (e.g., unpolarized and polarized) to provide a 'master' average spectrum. This master
230 average spectrum was used to determine hydrogen concentrations as well as to calculate
231 concentration ratios for each phase and for each duration condition. Since new IR calibration
232 could be proposed in the future, we also reported the normalized integrated absorbance for each
233 average master spectrum.

234 The FTIR spectra for the starting material are shown in Figure 2. The main IR bands are
235 located at 3572, 3594 and 3634 cm^{-1} for ol, opx and cpx respectively. Garnet did not show any
236 OH band and is then considered dry. The observed OH bands are typical hydrolyzed defects of
237 mantle-derived NAMs (see Miller et al., 1987; Bell and Rossmann, 1992; Ingrin and Skogby,

2000; Demouchy and Bolfan-Casanova, 2016). The hydrogen concentrations in NAMs in the starting material (lherzolitic material) are homogeneous from grains to grains. From the average MIR spectra, the averaged hydrogen concentrations of the starting material are 5, 186 and 286 ppm H_2O wt in ol, opx and cpx respectively, using the calibration of Paterson (1982) and 8, 201 and 422 ppm H_2O wt in ol, opx and cpx respectively, using the mineral-dependent calibrations (Bell et al., 1995; Withers et al., 2012). These values are in agreement with previous reports by Demouchy (2004) for the same garnet-bearing peridotite xenolith from Patagonia (Chile).

Results

The experimental conditions are reported in Table 1 and the concentrations in hydrogen are compiled in Table 2.

After annealing at 3 GPa and 1100 °C, thermal quench, decompression and sample preparation, the capsules display several horizontal fractures, but also large crystal portions which can be analyzed by FTIR as shown by Figure 3. Neither melt film, nor melt lens, nor melt pockets are visible at the sides or top of the capsule or between mineral grains, in reflective light to the contrary to Aubaud et al., (2004); Bali et al., (2008); Tenner et al., (2009); Withers et al., (2011), Férot and Bolfan-Casanova, (2012); Novella et al., (2015), demonstrating that the hydrogenated annealing conditions were subsolidus, as expected. Crystallization of new minerals is not observed.

The FTIR spectra of the hydrogenated NAMs are displayed in Figure 4. The main OH bands in olivine are the same as in the olivine from the starting material, but they have different intensities (Fig. 3 and 4a). Irrespective of annealing duration, the master spectrum of olivine, as defined in the previous section, shows dominant OH bands at 3612, 3572, 3525, 3352, 3328 and 3228 cm^{-1}. For orthopyroxene, the master spectrum also shows an increase of intensity from the

starting material with three dominant OH bands at 3595, 3520 and 3420 cm^{-1} (and minor bands at 3305 and 3060 cm^{-1}). The spectrum changes after annealing, the band at 3420 cm^{-1}being as high or higher than the peak at 3596 cm^{-1} which was dominant in the initial spectrum. The same modification was previously reported by Stalder and Skogby (2007). For clinopyroxene, the increase in intensity is global when compared to the starting material. The OH band at 3635 cm^{-1} remains the major IR band. Note that none of the spectrum displays evidence of contamination by molecular water and/or nano-inclusions containing water-derived species (see Keppler and Rauch, 2000 or Demouchy et al., 2012 for spectra comparison).

In all cases (duration and mineral phases), the intensity of each band is significantly higher than in the starting material, confirming significant hydrogenation during annealing (Fig 2 and 4). The difference between the spectra after annealing at 10, 25 or 100 hours is not exceeding the range of minimum and maximum values obtained for each set of spectra (see details in Table 2). Indeed, the post-annealing absorption coefficient normalized to the absorption coefficient of the starting material as shown in Figure 5, is almost constant for the 3 annealing durations (10, 35 and 100 hours). It confirms that the talc-pyrex cell from the piston-cylinder assembly provides an efficient flux of H to the system and enables modification of the initial hydrogen concentration. The increase in absorbance results from hydrogen incorporation and the initial hydrogen concentration is increased by a factor of 13 for olivine, and 3 for both pyroxenes, as shown in Fig. 5.

The application of the mineral-dependent calibrations (Bell et al., 1995, Withers et al., 2012, and described above) to each NAMs for each experiment enables the quantification of the hydrogen concentrations and yields 115 (107-126) ppm H_2O wt for olivine, 635 (568-716) ppm H_2O wt for opx and 1214 (1128-1372) ppm H_2O wt for cpx (Table 2 and Figure 4). At 3 GPa and 1100°C, for a peridotite containing 68% of olivine, 19 % of opx, 12% of cpx and 2% of garnet

(calculated using mineral proportion of the initial minerals mixed in the capsules), the bulk H concentration in the current melt-free peridotite is 342 ppm wt H_2O (range: 327-469 ppm H_2O wt). The bulk hydrogen concentration is 4 times higher than in the starting peridotite (94 ppm wt H_2O, using the same calibration, Withers et al., 2012 and Bell et al., 1995 and mineral modes). If modal proportion in an average peridotite from a recent data compilation is used (i.e., containing 67% of olivine, 22 % of opx, 10% of cpx and 2% of garnet, from Demouchy and Bolfan-Casanova, 2016), the bulk H concentration is 338 ppm wt H_2O (range: 309-379 ppm H_2O wt).

Discussion

FTIR spectra

The NAMs IR bands from the annealed experiments (Fig. 4) are in agreement with previous experimental studies focusing on hydrogen incorporation in NAMs at saturation level at high pressure, high temperature and for mantle composition (e.g., for olivine: Kohlstedt et al., 1996; Férot and Bolfan-Casanova, 2012; Demouchy et al., 2016; e.g., for pyroxenes: Stalder and Skogby, 2003; Stalder et al., 2005). The IR band positions (Fig. 4) are also in agreement with results obtained from mantle-derived samples displaying high hydrogen concentrations for olivine (e.g., Miller, et al., 1987; Ingrin and Skogby, 2000; Peslier, 2010; Demouchy and Bolfan-Casanova, 2016) as well as for pyroxenes (e.g., Skogby and Rossman, 1989; Skogby et al., 1990; Ingrin and Skogby, 2000; Skogby, 2006; Xia et al., 2013; Hess et al., 2015; Bizimis and Peslier, 2015; Demouchy and Bolfan-Casanova, 2016). Therefore, even if only H was used as a dopant (i.e., ionic diffusion of H and no molecular H_2O or hydrous minerals in the capsule), we interpret the results of our hydrogen incorporation experiments as relevant to address the water storage in NAMs of the Earth's upper mantle.

Hydrogen concentration

The bulk H concentration of a standard peridotite (67% ol, 22 % opx, 10% cpx, 2% garnet), calculated from the current subsolidus experiments, is ~ 340 ppm wt H_2O. This bulk value is a factor ~7 higher than values observed at 3 GPa in natural peridotite specimens, when using the same mineral-dependent IR calibrations. Indeed, a recent compilation by Demouchy and Bolfan-Casanova (2016) indicates that at 3 GPa (80-120 km of depth, number of xenoliths =10), NAMs contain in average 5, 104, and 234 ppm wt H_2O for olivine, orthopyroxene and clinopyroxene, respectively. It thus yields a bulk H concentration of 50 ppm wt H_2O (i.e., same mineral modes as above, and same mineral-dependent calibration). The discrepancy between the bulk hydrogen concentration in natural specimens and the results of our experiments is significant and the concentration gap is higher than that observed for one single geological setting (i.e., off- or on-craton, bulk between 8 and 153 ppm wt H_2O at 110 km of depth, data compilation from Demouchy and Bolfan-Casanova, 2016). We make the assumption that the limited amount of hydrogen observed in mantle specimens is mostly due to dehydration during partial melting (in an open system) at depth or during ascent towards the surface, which could have lower the hydrogen fugacity in the system and modified an originally higher hydrogen concentration primary resulting from cryptic or stealth metasomatism (i.e., Demouchy et al., 2015).

The successful hydrogenation of olivine and pyroxenes is at odd with the dryness of garnet in this study. Mantle-derived garnets were reported to contain limited amount of hydrogen (e.g., Peslier, 2010), but not in a systematic way (e.g., Demouchy et al., 2015). Here the garnet grains are dry after annealing, it could be due the detection limit (grains are too small) or to a composition effect (Beran and Libowitzky, 2006).

333

334 *Subsolidus partition coefficients*

335 The bulk water content is 0.009 wt.% H_2O in the initial peridotite and equals to 0.034
336 wt.% H_2O after hydrogenation. At a pressure of 3 GPa, and at 1 100°C and for bulk water content
337 between 0 and 0.05 wt.% H_2O, the models of Katz et al., (2003) indicate the absence of melting
338 (see their figure 3). Other models, based on experimental petrology, predicted melting and/or
339 precipitation of pargasite, but in water-rich systems (e.g., Grove et al., 2006; 14.5 wt.% H_2O in
340 the bulk) or at lower pressure conditions (water-poor system at 2.5 GPa, Green et al., 2014). In
341 this study, the H concentrations in NAMs are high, and remain just below water saturation (e.g.,
342 Férot and Bolfan-Casanova, 2012; Demouchy and Bolfan-Casanova, 2016). If melt was present
343 in the capsule, a significant drop in hydrogen concentration would have been observed compared
344 to water-saturation values (see e.g., Bali et al., 2008; Férot and Bolfan-Casanova, 2012), which is
345 not the case here. Thus, melting model for water-poor systems (<0.05 wt.% H_2O) and the
346 reported high hydrogen concentrations in the NAMs (0.0350 wt.% H_2O in bulk) both settle again
347 the subsolidus status of the present experiments.

348 From the experimental conditions and the size of the minerals, 10 hours are long enough
349 to modify the hydrogen concentrations to a new hydrogen fugacity at 3 GPa and 1100 °C (Figure
350 5) for all NAMs grains (i.e., ranging from 1 mm for olivine to the small 300-200 micron
351 clinopyroxenes). Since the hydrogen concentration remains constant for the three annealing
352 durations in all mineral phases (within error bars), the system can be considered at equilibrium
353 regarding hydrogen concentrations. The inter-mineral hydrogen concentration ratios can therefore
354 be taken as accurate partition coefficients for the given pressure and temperature conditions (3
355 GPa, 1100 °C). It yields $D_{opx/ol}$=5±1, $D_{cpx/ol}$= 10±2, and $D_{cpx/opx}$=1.9±0.4, as reported in Table 3
356 and displayed in Figure 6. The apparent partition coefficient of hydrogen between the two

pyroxenes is constant, and around 2, both after annealing and in the starting material, while the partition coefficients between olivine and pyroxenes are significantly smaller than in the lherzolitic protolith (from $D_{initial\ opx/ol} \approx 24$ down to $D_{final\ opx/ol} \approx 5$, and from $D_{initial\ cpx/ol} \approx 53$ down to $D_{final\ cpx/ol} \approx 10$, see Table 3 for $D_{final\ min/min}$ calculated using other IR calibrations). These results lead to the following conclusions regarding hydrogen distribution under subsolidus conditions: (1) it confirms that the very high diffusivity of hydrogen in olivine induces rapid intake to new higher hydrogen fugacity than experienced at depth, and implies that olivine is indeed an unreliable recorder of original mantle hydrogen content, even when co-existing with other NAMs. The same conclusion was previously reached from studies on natural peridotites (e.g., Demouchy et al., 2006; Peslier and Luhr, 2006; Denis et al., 2013), and suggested from ionic diffusion experiments in single crystals of olivine and pure forsterite (Mackwell and Kohstedt, 1990; Demouchy and Mackwell, 2003; 2006; Padron-Navarta et al., 2014; Demouchy et al., 2016). It is the first time that it is directly observed from experiments where co-existing NAMs are subjected to a H flux, that is to say to H diffusion only. (2) The current results also settle the hydrogen partition coefficient between the two pyroxenes to ≈ 2, as previously inferred from data compilation on natural specimens (Peslier et al., 2002; Xia et al., 2010; Denis et al., 2015; see Peslier et al., 2010 and Demouchy and Bolfan-Casanova for reviews). This factor of 2 appears to hold even if the hydrogen concentrations are modified rapidly and increase by a factor 3 within only 10 hours of annealing. It thus questions both pyroxenes as reliable hydrogen recorders as well. However, the partition coefficient between opx and cpx seems to be a very steady feature whatever the pressure and temperature conditions, the bulk hydrogen content or the presence of melt. It could therefore be used to assess equilibrium conditions in natural samples or experimental charges where opx and cpx have behaved differently, as it is the case for the crystallization of secondary metasomatic cpx during stealth metasomatism for example.

The new partition coefficients are compared to previous experimental results and concentration ratios obtained from natural samples in Table 3. The projections from Hirth and Kohstedt (1996) are in strikingly good agreement with the results of this study. Nonetheless, results from experiments where all three NAMs (ol, opx and cpx) are present in the experimental specimens and were analysed, are dissimilar from our results (Table 3). Note that in most of the other studies, the NAMs are neo-formed solid phases at equilibrium, always co-existing with a large amount of water-rich silicate melt and/or other neo-formed minerals (i.e., pargasite, Kovács et al., 2012). From the data compilation, the $D_{cpx/opx}$ is the coefficient with the smallest variability and a value ≈ 2 (Table 3). The $D_{cpx/ol}$ values are the most heterogeneous, ranging from $D_{cpx/ol} = 33$ (Tenner et al., 2009) down to $D_{cpx/ol} = 3.3$ for experiments at higher pressure (6 GPa, Novella et al., 2014) and from $D_{cpx/ol} = 176$ to 37 for natural samples (Bell and Rossmann, 1992). The $D_{opx/ol}$ values have smaller variability, and range from 12.2 (Hauri et al., 2006) down to 1.8 (Novella et al., 2014). Again, natural samples display a large heterogeneity with $D_{opx/ol}$ values ranging from 62 to 18 (Bell and Rossmann, 1992). While the values from Bell and Rossmann (1982) can be altered, as they did not use mineral-specific calibrations at that time, the same variability in $D_{opx/ol}$ is described in the data compilation by Peslier et al., (2010) and Demouchy and Bolfan-Casanova (2016). We attribute the diversity of $D_{px/ol}$ in natural samples to significant but incomplete loss of hydrogen in olivine (e.g., Demouchy et al., 2006; Peslier and Luhr, 2006; Denis et al., 2013; Peslier et al 2015). The variability in the data from experiments in laboratory can be attributed to important variations in pressure range, precision of the secondary ion mass spectrometer (SIMS), quality of the standards used for the SIMS calibration curves, and stability/reproducibility of the vacuum (i.e., Mosenfelder et al., 2011; Withers et al., 2011). Nevertheless, the most recent study by Novella et al., (2014), where two independent quantitative techniques were used (SIMS and Elastic Recoil Detector analyses), provides the most reliable partition coefficients

405 asthenospheric mantle (6 GPa, 180 km of depth, low Al-pyroxenes) when water-rich silicate melt
406 is present. The study presented here illustrates the need for melt-free and melt-bearing inter-
407 mineral partition coefficients for hydrogen at realistic lithospheric conditions.
408
409 *H loss in peridotite*
410 Even if hydrogen under-saturation of the uppermost mantle, induced by partial melting, is
411 a reasonable hypothesis, we must discuss an alternative, which is an important hydrogen loss in
412 NAMs during (late) sub-surface processes (e.g., melt extraction, magma chamber dynamics,
413 transport to the surface, fast decompression and lava flow cooling) in natural samples. The
414 hydrogen loss was especially reported for olivine (Demouchy et al., 2006; Peslier and Luhr,
415 2006; Denis et al., 2013; see also Lloyd et al., 2012; 2016; Biró et al. 2016 for dehydration in
416 other NAMs)). However, the discrepancy between bulk concentrations calculated from the
417 present experiments and from natural samples cannot be attributed solely to H loss in olivine.
418 Partial depletion of pyroxenes must also occur and participate to lower the bulk hydrogen
419 concentration observed in mantle peridotites. This hypothesis of a significant hydrogen loss in
420 opx has indeed recently been reported by Tian et al., (2016) in peridotite xenoliths from China.
421 Nonetheless, many other studies did not report systematic hydrogen loss in ortho- or
422 clinopyroxenes (see Demouchy and Bolfan-Casanova for full list of references), leaving the
423 reasons of the preservation from dehydration (e.g., caught–in-the-act) in NAMs unexplained and
424 calling for more systematic line analyses (by FTIR or SIMS) in H-rich and H-poor pyroxenes.
425 Moreover, if mechanisms of dehydration are somehow different than hydration (or re-hydration
426 of pre-existing defects), pyroxenes could indeed behave as a reliable H recorder, then our new
427 subsolidus partition coefficients could be used to calculate the initial hydrogen concentration in

olivine before transport towards the surface. It might be of particular importance for olivine, which is controlling the rheology of the upper mantle.

Implications

The results of this experimental study point out the requirement to establish melt-free inter mineral partition coefficients for hydrogen, for a wide range of pressure and temperature, especially under lithospheric conditions (i.e., temperature lower than a mantle adiabat) and for chemical composition relevant to Earth's mantle only. Our hydration experiments question the reliability of both pyroxenes and olivine as hydrogen recorders. Further studies are required to decipher hydration and dehydration mechanisms since they may not be symmetrical (Thoraval and Demouchy, 2014). Indeed several crystal defects are involved, and must interplay during diffusion out hydrogen in NAMs.

At last, our results imply that the mere use of partition coefficients derived from melt-rich high pressure experiments could lead to misunderstanding of hydrogen distribution at depth when applied to mantle-derived rocks equilibrated at subsolidus temperatures.

Acknowledgments

The authors thank the associated editor and two reviewers for very constructive comments. S.D. deeply thanks J.-A. Padròn-Navarta for fruitful discussion on peridotite melting curves, H. Schulze for outstanding capsule polishing, H. Fisher for perfect capsule manufacture, and D. Maurin for the management of the FTIR lab at the University of Montpellier. This study was financially supported by DFG Core facility: High-pressures laboratories of Bayerisches Geoinstitut, Bayreuth University, Germany (KE501/10-1).

References

Ardia, P., Hirschmann, M.M., Withers, A.C., , and Tenner, T.J., (2012) H_2O storage capacity of olivine at 5–8GPa and consequences for dehydration partial melting of the upper mantle. Earth and Planetary Science Letters, 345-348, 104–116.

Asimow, P.D., Hirschmann, M.M., and Stolper, E.M., (2001) Calculation of peridotite partial melting from thermodynamic models of minerals and melts, IV: Adiabatic decompression and the composition and mean properties of mid-ocean ridge basats. Journal of Petrology, 42, 963–998.

Asimow, P.D., Stein, L. C., Mosenfelder, J., L., and Rossman, G. R., (2006) Quantitative polarized infrared analysis of trace OH in populations of randomly oriented mineral grains. American Mineralogist, 91, 278–284.

Aubaud, C., Hauri, E., and Hischmann, M.M., (2004) Hydrogen partition coefficients between nominally anhydrous minerals. Geophysical Research Letters, 31, doi:10.1029–2004GL021341.

Aubaud, C., Hirschmann, M.M., Withers, A.C., and Hervig, R.L., (2008) Hydrogen partitioning between melt, clinopyroxene, and garnet at 3 GPa in a hydrous MORB with 6 wt% H_2O. Contribution to Mineralogy and Petrology, 156, 607–625.

Bali, E., Bolfan-Casanova, N., and Koga, K., (2008). Pressure and temperature dependence of H solubility in forsterite: an implication to water activity in the Earth interior. Earth and Planetary Science Letters, 268, 354–363.

Bell, D.R., and Rossman, G.R., (1992) Water in Earth's mantle: The role of nominally anhydrous minerals. Science, 255, 1391–1397.

475 Bell, D.R., Ihinger, P.D., and Rossman, G.R., (1995) Quantitative and analysis of trace OH in
476 garnet and pyroxenes. American Mineralogist, 80, 465–474
477 Bell, D.R., Rossman, G.R., Moore, R.O. (2004): Abundance and partitioning of OH in a high-
478 pressure magmatic system: megacrysts from the Monastery kimberlite, South Africa.
479 J. Petrol., 45, 1539–1564.
480 Beran A., and Libowitzky E., N., (2006) Water in natural mantle minerals II: Olivine, garnet and
481 accessory minerals. Reviews in Mineralogy and Geochemistry, 62, 193–230.
482 Biró, T., Kovács, I.J., Király, E., Falus, G., Karátson, D., Bendo, Z., Fancsik, T., and Sándorné,
483 J.K., (2016) Concentration of hydroxyl defects in quartz from various rhyolitic ignimbrite
484 horizons: results from unpolarized micro-FTIR analyses on unoriented phenocryst
485 fragments. European Journal of Mineralogy, 28, 313–327.
486 Bizimis, M., Peslier, A.H., (2015). Water in Hawaiian garnet pyroxenites: Implications for water
487 heterogeneity in the mantle. Chemical Geology 397, 61–75.
488 Bolfan-Casanova, N., Keppler, H., and Rubie, D.C., (2000). Water partitioning between
489 nominally anhydrous minerals in the MgO-SiO_2-H_2O system up to 24 GPa:
490 Implications for the distribution of water in the Earth's mantle. Earth and Planetary Science
491 Letters, 182, 209–221.
492 Bose, K., and Ganguly, J., (1995) Quartz-coesite transition revisited: reversed experimental
493 determination at 500–1200°C and retrieved thermochemical parameters.
494 American Mineralogist, 80, 231–238.
495 Brey, G.P., and Köhler, T., (1990). Geothermobarometery in four-phase lherzolith II. New
496 thermobarometrers, and practical assessment of existing thremobarometers. Journal
497 of Petrology, 31, 1353–1378.

498 J., Kufudakis, A., and Gardavska G., 1979. Diffusivity of hydrogen in platinum and
Cermak 499 the diffusion-elestic phenomenon. Journal of Less-Common Metals, 63, 1-8.
500 Costa, F., and Chakraborty, S., (2008) The effect of water in Si and O diffusion rates in olivine
501 and implications for the transport properties and processes in the upper mantle. Physic
502 of the Earth and Planetery Interior, 166, 11–29.
503 Demouchy, S., (2004) Thermodynamics and kinetics of hydrogen incorporation in olivine and
504 wadsleyite, Bayerisches Geoinstitut. Bayreuth University, Bayreuth.
505 Demouchy, S., and Bolfan-Casanova, N., (2016) Distribution and transport of hydrogen in the
506 lithospheric mantle: A review. Lithos, 240-243, 402–425.
507 Demouchy, S., and Mackwell, S., (2006) Mechanisms of hydrogen incorporation and diffusion in
508 iron-bearing olivine. Physics and Chemistry of Minerals, 33, 347–355.
509 Demouchy, S., and Mackwell, S.J., (2003) Water diffusion in synthetic iron-free forsterite.
510 Physics and Chemistry of Minerals, 30, 486–494.
511 Demouchy, S., Jacobsen, S.D., Gaillard, F., and Stern, C.R., (2006) Rapid magma ascent
512 recorded by water diffusion profiles in mantle olivine. Geology, 34, 429–432.
513 Demouchy, S., Mackwell, S.J., and Kohlstedt, D.L., (2007) Influence of hydrogen on Fe–Mg
514 interdiffusion in (Mg,Fe)O and implications for Earth's lower mantle. Contribution
515 to Mineralogy and Petrology, 154, 279–289
516 Demouchy, S., Tommasi, A., Barou, F., Mainprice, D., and Cordier, P., (2012) Deformation of
517 olivine in torsion under hydrous conditions. Physics of Earth and Planetary Interiors,
518 202-203, 57–70.
519 Demouchy, S., Ishikawa, A., Tommasi, A., Alard, O., and Keshav, S., (2015) Characterization of
520 hydration in the mantle lithosphere: Peridotite xenoliths from the Ontong Java Plateau as
521 an example. Lithos, 212-215, 189–201.

Demouchy, S., Thoraval, C., Bolfan-Casanova, N., and Manthilake, G., (2016) Diffusivity of hydrogen in iron-bearing olivine at 3GPa. Physics of Earth and Planetary Interiors, 260, 1–13.

Denis, C.M.M., Demouchy, S., and Shaw, C., (2013) Evidence of dehydration in peridotites from Eifel Volcanic Field and estimates of magma ascent rates. Journal of Volcanology and Geothermal Research, 258, 85–99.

Denis, C.M.M., Alard, O., and Demouchy, S., (2015). Water content and hydrogen behaviour during metasomatism in the uppermost mantle beneath Ray Pic volcano (Massif Central, France). Lithos, 236-237, 256–274.

Dobson, P.F., Skogby, H., and Rossman, G.R. (1995) Water in boninite glass and coexisting orthopyroxene: Concentration and partitioning, Contribution to Mineralogy and Petrology, 118, 414–419.

Férot, A., and Bolfan-Casanova, N., (2012) Water storage capacity in olivine and pyroxene to 14 GPa: Implications for the water content of the Earth'supper mantle and nature of seismic discontinuities. Earth and Planetary Science Letters, 349-350, 218–230.

Ferriss, E., Plank, T., Walker, D., and Nettles, M., (2015) The whole-block approach to measuring hydrogen diffusivity in nominally anhydrous minerals. American Mineralogist, 100, 837–851.

Ferriss, E., Plank, T., and Walker, D., (2016) Site-specific hydrogen diffusion rates during clinopyroxene dehydration. Contribution to Mineralogy and Petrology, 171-55, doi : 10.1007/s00410-016-1262-8

Frost, D.J., and McCammon, C.A., (2008) The Redox State of Earth's Mantle. Annual Review in Earth and Planetary Sciences, 36, 389–420.

Gaetani, G.A., and Grove, T.L., (1998) The influence of water on melting of mantle peridotite. Contribution to Mineralogy and Petrology, 131, 323–346.

Gaetani, G.A., O'Leary, J.A., Koga, K.T., Hauri, E.H., Rose-Koga, E.F., and Monteleone, B.D., (2014) Hydration of mantle olivine under variable water and oxygen fugacity conditions. Contribution to Mineralogy and Petrology, 167, 965.

Gasc, J., Brunet, F., Brantut, N., Corvisier, J., Findling, N., Verlaguet, A., and Lathe, C. (2016) Effect of water activity on reaction kinetics and intergranular transport : insights from the Ca(OH)(2) + $MgCO_3$→$CaCO_3$ + Mg(OH)(2) reaction at 1.8 GPa. Journal of Petrolology, 57 (7), 1389-1407.

Grant, K., Ingrin, J., Lorand, J.P., and Dumas, P., (2007) Water partitioning between mantle minerals from peridotite xenoliths. Contribution to Mineralogy and Petrology, 154, 15–34.

Green, D.H, Hibberson, W.O., Rosenthal, A., Kovács, I, Yaxley, G.M., Falloon, T.J., and Brink F., (2014) Experimental study of the influence of water on melting and phase assemblages in the upper mantle. Journal of Petrology, 55(10):2067–2096.

Grove, T., Chatterjee, N., Parman, S., and Medard, E., (2006) The influence of H_2O on mantle wedge melting. Earth and Planetary Science Letters, 249, 74–89.

Hauri, E., Gaetani, G.A., and Green, T.H., (2006) Partitioning of water during meting of the Earth's upper mantle at H_2O-undersaturated conditions. Earth and Planetary Science Letters, 248, 715-734.

Hesse, K.T., Gose, J., Stalder, R., Schmädicke, E., (2015). Water in orthopyroxene from abyssal spinel peridotites of the East Pacific Rise (ODP Leg 147: Hess Deep). Lithos, 232, 23–

Hier-Majumder, S., Anderson, I.M., and Kohlstedt, D.L., (2004) Influence of Protons on Fe-Mg interdiffusion in olivine. Journal of Geophysical Research. 110, B02202, doi: 10.1029–2004JB003292.

569 Hirschmann, M., (2010) Partial melt in the oceanic low velocity zone. Physics of Earth and
570 Planetary Interiors, 179, 60–71.
571 Hirschmann, M., Aubaud, C., and Withers, A.C., (2005). Storage capacity of H_2O in nominally
572 anhydrous minerals in the upper mantle. Earth and Planetary Science Letters, 236, 167–181.
573 Hirschmann, M.M., Tenner, T., Aubaud, C., and Withers, A.C., (2009) Dehydration melting of
574 nominally anhydrous mantle: The primacy of partitionning. Physics of Earth and
575 Planetary Interiors, 176, 54–68.
576 Hirth, G., and Kohlstedt, D.L., (1996) Water in the oceanic upper mantle: implications for
577 rheology, melt extraction and the evolution of the lithosphere. Earth and Planetary
578 Science Letters, 144, 93–108.
579 Ingrin, J., and Skogby, H., (2000) Hydrogen in nominally anhydrous upper-mantle
580 minerals: concentration levels and implications. European Journal of Mineralogy, 12, 543–570.
581 Inoue, T., Weidner, D.J., Northrup P.A., and Parise JB, (1998). Elastic properties of hydrous
582 ringwoodite (γ-phase) in Mg_2SiO_4. Earth and Planetary Science Letters, 160, 107–113.
583 Jacobsen, S.D., (2006) Effect of water on the equation of state of nominally anhydrous minerals.
584 Reviews in Mineralogy and Geochemistry 62, 321–342.
585 Jacobsen, S.D., Smyth, J.R., Spetzler, H.A., and Frost, D.J., (2004) Sound velocities and elastic
586 constant of iron-bearing hydrous ringwoodite. Physics of Earth and Planetary Interiors,
587 143-144, 47–56.
588 Karato, S.I., (1990). The role of hydrogen diffusivity in the electrical conductivity of the upper
589 mantle. Nature, 347, 272–273.
590 Karimova, A, and Stalder, R. (2013) OH in diopside and enstatite at 6 GPa in the system CaO–
591 MgO–SiO_2–H_2O, European Journal of Mineralogy. 2013, 25, 299–305

592 Katz, R.F., Spiegelman, M., and Langmuir, C.H., (2003) A new parameterization of hydrous
593 mantle melting. Geochemistry, Geophysics and Geosystems, 4
594 (9), doi:10.1029/2002GC000433.
595 Keppler, H., and Rauch, M., 2000. Water solubility in nominally anhydrous minerals measured
596 by FTIR and ^{1}H MAS NMR: Effect of sample preparation. Physics and Chemistry
597 of Minerals, 27, 371–376.
598 Koga, K., Hauri, E., Hirschmann, M., and Bell, D.R., (2003) Hydrogen concentration analysis
599 using SIMS and FTIR: Comparison and calibration for nominally anhydrous
600 minerals. Geochemistry, Geophysics and Geosystems, 4, 1019–doi: 10.1029–
601 Kohlstedt, D.L., (2006). The role of water in high-temperature rock deformation. Reviews in
602 Mineralogy and Geochemistry 62, 377–396.
603 Kohlstedt, D.L., Keppler, H., and Rubie, D.C., (1996) Solubility of water in the α, β and γ phases
604 of $(Mg,Fe)_2SiO_4$. Contribution to Mineralogy and Petrology, 123, 345–357.
605 Kovàcs, I., Hermann, J., O'Neill, H.S.C., Fitz Gerald, J.D., Sambridge, M., and Horvàth, G.,
606 (2008) Quantitative absorbance spectroscopy with unpolarized light: Part II.
607 Experimental evaluation and development of a protocol for quantitative analysis of
608 mineral IR spectra. American Mineralogist, 93, 765–778.
609 Kovàcs, I., Green, H.W., Rosenthal, A., Hermann, J., O'Neill, H.S.C., Hibberson, W.O., and
610 Udvardi, B., (2012). An experimental study of water in nominally anhydrous minerals
611 in the upper mantle near water-saturated solidus. Journal of Petrology, 53, 2067–2093.
612 Li, Y., Wiedenbeck, M., Shcheka, S., and Keppler, H., (2013) Nitrogen solubility in upper mantle
613 minerals. Earth and Planetary Science Letters, 377–378 (2013) 311–323.

614 Libowitzky, E., Rossman, G.R., (1997) An IR absorption calibration for water in minerals.
615 American Mineralogist, 82, 1111–1115.
616 Lloyd, A.S., Plank, T., Ruprecht, P., Hauri, E.H., and Rose, W., (2012). Volatile loss from melt
617 inclusions in pyroclasts of differing sizes. Contribution to Mineralogy and Petrology, 165,
618 129–153.
619 Lloyd, A.S., Ferriss, E., Ruprecht, P., Hauri, E.H., Jicha, B.R., and Plank, T., (2016) An
620 Assessment of Clinopyroxene as a Recorder of Magmatic Water and Magma Ascent Rate.
621 Journal of Petrology 57, 1865–1886.
622 Mackwell, S.J., and Kohlstedt, D.L., (1990) Diffusion of hydrogen in olivine: Implications for
623 water in the mantle. Journal of Geophysical Research, 95, 5079–5088.
624 Mackwell, S.J., Kohlstedt, D.L., and Paterson, M.S., (1985) The role of water in the deformation
625 of olivine single crystals. Journal of Geophysical Research, 90, 11–319–11–333.
626 McCammon, C.A., (2005) The paradox of mantle redox. Science, 308, 807–807.
627 Miller, G.H., Rossman, G.R., and Harlow, G.E., (1987) The natural occurence of hydroxide in
628 olivine. Physics and Chemistry of Minerals, 14, 461–472.
629 Mosenfelder, J.L., Deligne, N.I., Asimow, P.D., and Rossman, G.R., (2006) Hydrogen
630 incorporation in olivine from 2-12 GPa. American Mineralogist, 91, 285–294.
631 Mosenfelder, J.L., LeVoyer, M., Rossman, G.R., Guan, Y., Bell, D.R., Asimow, P.D., and Eiler,
632 J.M., (2011) Analysis of hydrogen in olivine by SIMS: Evaluation of standards and
633 protocole. American Mineralogist, 96, 1725–1741.
634 Novella, D., Frost, D.J., Hauri, E.H., Bureau, H., Raepsaet, C., and Roberge, M., (2014) The
635 distribution of H_2O between silicate melt and nominally anhydrous peridotite and the onset
636 of hydrous melting in the deep upper mantle. Earth and Planetary Science Letters, 400, 1–
637 13.

638 Padrón-Navarta, J.A., Hermann, J., and O'Neill, H.S.C., (2014) Site-specific hydrogen diffusion
639 rates in forsterite. Earth and Planetary Science Letters, 392, 100–112.
640 Paterson, M.S., (1982) The determination of hydroxyl by infrared absorption in quartz, silicate
641 glasses and similar materials. Bulletin de Minéralogie, 105, 20–29.
642 Peslier, A.H., (2010) A review of water contents of nominally anhydrous minerals in the mantles
643 of Earth, Mars and the Moon. Journal of Volccanology and Geothermal Reseach, 197,
644 239–258.
645 Peslier, A.H., and Luhr, J.F., (2006) Hydrogen loss form olivines in mantle xenoliths from sincoe
646 (USA) and Mexico: mafic alkalic magma ascent rate and water budget of the
647 sub-continental lithosphere. Earth and Planetary Science Letters, 242, 302–314.
648 Peslier, A.H., Luhr, J.F., and Post, J., (2002) Low water contents in pyroxenes from spinel-
649 peridotites of the oxidized, sub-arc mantle wedge. Earth and Planetary Science Letters,
650 201, 69–86.
651 Peslier, A.H., Bizimis, M., and Matney, M., (2015) Water disequilibrium in olivines from
652 Hawaiian peridotites: Recent metasomatism, H diffusion and magma ascent
653 rates. Geochimica et Cosmochimica Acta, 154, 98-117.
654 Shuai, K., and Yang X. (2017) Quantitative analysis of H-species in anisotropic minerals by
655 polarized infrared spectroscopy along three orthogonal directions. Contribution to
656 Mineralogy and Petrology, 172,14.
657 Skogby, H., (2006) Water in natural mantle minerals I: Pyroxenes. Reviews in Mineralogy and
658 Geochemistry, 62, 155–167.
659 Skogby, H., Rossman, G.R., (1989) OH-in pyroxene: An experimental study of incorporation
660 mechanisms and stability. American Mineralogist, 74, 1059–1069.

661 Skogby, H., Bell, D.R., Rossman, G.R., (1990) Hydroxide in pyroxene: Variations in the natural
662 environment. American Mineralogist, 75, 764–774.
663 Sokol, A.G., Kupriyanov, I.N., Palyanov, Y.N., Kruk, A.N., and Sobolev, N.V., (2013) Melting
664 experiments on the Udachnaya kimberlite at 6.3-7.5 GPa: Implications for the role of H_2O
665 in magma generation and formation of hydrous olivine. Geochimica et Cosmochimica Acta
666 101, 133–155.
667 Sokol, A.G., Kruk, A.N., and Palyanov, Y.N., (2014) The role of water in generation of group II
668 kimberlite magmas: Constraints from multiple saturation experiments.
669 American Mineralogist, 99, 2292–2302.
670 Stalder, R. & Behrens, H. (2006) D/H exchange in pure and Cr-doped enstatite: implications for
671 hydrogen diffusivity. Physics and Chemistry of Minerals 33, 601-611.
672 Stalder, R. & Skogby, H. (2003) Hydrogen diffusion in natural and synthetic orthopyroxene.
673 Physics and Chemistry of Minerals 30, 12-19.
674 Stalder, R. & Skogby, H. (2007) Dehydration mechanisms in synthetic Fe-bearing enstatite. Eur.
675 J. Mineral. 2007, 19, 201–216
676 Stalder, R., Klemme, S., Ludwig, T., Skogby, H., (2005) Hydrogen incorporation in
677 orthopyroxene: interaction of different trivalent cations. Contribution to Mineralogy and
678 Petrology 150, 473–485.
679 Stern, C.R., Kilian, R., Olker, B., Hauri, E.H., and Kurtis Kyser, T., (1999) Evidence from mantle
680 xenoliths for relatively thin (<100 km) continental lithosphere below the Phanerozoic crust
681 of southernmost South America. Lithos, 48, 217–235.
682 Sweeney, R.J., Prozesky, V.M. and Springhorn, and K.A., (1995) Use of elastic recoil detection
683 analysis (ERDA) microbeam technique for the quantitative determination of hydrogen in

materials and hydrogen partitioning between olivine and melt at high pressures, Geochimica et Cosmochimica Acta, 61, 101–113, 199.

Tasaka, M., Zimmerman, M.E., and Kohlstedt, D.L., (2016) Evolution of the rheological and microstructural properties of olivine aggregates during dislocation creep under hydrous condition, Journal of Geophysical Reseach, 121 , 92-113.

Tenner, T.J., Hirschmann, M.M., Withers, A.C., and Hervig, R.L., (2009) Hydrogen partitioning between nominally anhydrous upper mantle minerals and melt between 3 and 5 GPa and applications to hydrous peridotite partial melting. Chemical Geology, 262, 42–56.

Tian, Z.-Z., Liu, J., Xia, Q.-K., Ingrin, J., Hao, Y.-T., and Christophe, D., (2016) Water concentration profiles in natural mantle orthopyroxenes: A geochronometer for long annealing of xenoliths within magma. Geology, G38620.1.

Thoraval, C., and Demouchy, S., (2014) Numerical models of ionic diffusion in one and three dimensions: application to dehydration of mantle olivine. Physics and Chemistry of Minerals 41, 709–723.

Wimmer, E., Wolf, W., Sticht, J., and Saxe, P., (2008) Temperarture-dependent diffusion coefficients from ab initio computations: hydrogen, deuterieum, and tritium in nickel. Physical Review. B 77, 134305.

Withers, A.C., and Hirschmann, M.M., (2008) Influence of temperature, composition, silica activity and oxygen fugacity on the H_2O storage capacity of olivine at 8 GPa. Contribution to Mineralogy and Petrology,156, 595-605.

Withers, A.C., Hirschmann, M.M., and Tenner, T., (2011) The effect of Fe on olivine H_2O storage capacity: Consequences for H_2O in the Martian mantle. American Mineralogist, 96, 1039–1053.

Withers, A.C., Bureau, H., Raepsaet, C., and Hirschmann, M.M., (2012) Calibration of infrared spectroscopy by elastic recoil detection analysis of H in synthetic olivine. Chemical Geology, 334, 92–98.

Xia, Q.-K., Hao, Y., Li, P., Deloule, E., Coltorti, M., Dallai, L., Yang, X., and Feng, M., (2010) Low water content of the Cenozoic lithospheric mantle beneath the eastern part of the North China Craton. Journal of Geophysical Research, 115, B07207.

Xia, Q.-K., Hao, Y.-T., Liu, S.-C., Gu, X.-Y., Feng, M., (2013). Water contents of the Cenozoic lithospheric mantle beneath the western part of the North China Craton: Peridotite xenolith constraints. Gondwana Research 23, 108–118.

Yang, X., (2015) OH solubility in olivine in the peridotite–COH system under reducing conditions and implications for water storage and hydrous melting in the reducing upper mantle. Earth and Planetary Science Letters, 432, 199–209.

Yoshino, T., Matsuzaki, T., Yamashita, S., and Katsura, T., (2006) Hydrous olivine unable to account for conductivity anomaly at the top of the asthenosphere. Nature, 973–976.

Figure captions

Figure 1: Sketch of the capsule assembly used in the experimental study. Batch of nominally anhydrous minerals from a mantle-derived garnet-lherzolite are placed as layers in a welded metal capsule. See main text for details.

Figure 2: Average FTIR spectra (master spectrum, see main text and Fig. 1S for details) for each mineral phase in the starting material (mantle-derived lherzolite from Pali-Aike). The thick black spectrum is for olivine ; the thin black spectrum is for orthopyroxene and the thick grey spectrum is for clinopyroxene. All the spectra are normalized to 1 cm of thickness.

731

732 **Figure 3:** (a) Micrograph of a capsule after annealing at 3 GPa, 1100 °C, 100 hours (PSD6), in
733 reflective light. (b) Micrograph of a capsule after annealing at 3 GPa, 1100 °C, 100 hours (PSD6)
734 in cross-polarized light showing large sections of crystals suitable for FTIR analyses.

735 **Figure 4:** Average FTIR spectra (master spectrum, see main text for details) for each mineral
736 phase. The thick gray spectrum is the starting material, shown as reference, the thick black line is
737 for an annealing duration of 10 h, the thin black line is for an annealing duration of 25 h and the
738 dashed black line is for an annealing duration of 100 h for (a), olivine, (b) orthopyroxene and (c)
739 clinopyroxene. All the spectra are normalized to 1 cm of thickness.

740 **Figure 5:** Evolution of the absorption coefficients (absorbance normalized to a thickness of 1
741 cm) in the minerals divided by the absorption coefficients of the starting material as a function of
742 the duration of annealing. The thick black line is for olivine; thin black line is for orthopyroxene
743 and the thick grey line is for clinopyroxene.

744 **Figure 6:** Evolution of the hydrogen partition coefficient between minerals as a function the
745 duration of annealing. The thin black line is for clinopyroxene/olivine; dashed black line is for
746 orthopyroxene/olivine and the thick grey line is for clinopyroxene/orthopyroxene. The mineral-
747 dependent calibration was used for the partition coefficients calculation (see Table 2 and 3 for
748 details).

749

750 **Figure S1:** FTIR spectra for sample PSD4, set of spectra for NAMs showing the average
751 polarized spectrum (black) relative to the sets of polarized spectra (grey), and relative to the
752 unpolarized average spectrum (red) demonstrating that averaging a large set of polarized and
753 unpolarized spectra yields very similar result

754

This is a preprint, the final version is subject to change, of the American Mineralogist (MSA)
Cite as Authors (Year) Title. American Mineralogist, in press.
(DOI will not work until issue is live.) DOI: http://dx.doi.org/10.2138/am-2017-6089

Table 1. Compilation of the piston-cylinder (talc-pyrex cell) run conditions.

Run#	Pressure (GPa)	Temperature (°C)	Buffer	Assemblage	Duration (hours)	Thickness for FTIR µm
PSD4	3	1100	Ni-NiO	ol+opx+cpx+gt	10	271
PSD5	3	1100	Ni-NiO	ol+opx+cpx+gt	25	204
PSD6	3	1100	Ni-NiO	ol+opx+cpx+gt	100	368

780
781

782 **Table 2**. Normalized integrated absorbances (NIA) and hydrogen concentrations in NAMs from
783 the starting material (PSM) and the annealed samples at high pressures (PSM#). We used several
784 IR calibrations: the calibration of Paterson (1982), Bell et al., (1995) and Withers et al., (2012).

	Nb§	NIA *			Calib. of Paterson **			Calib. of Withers (ol) or of Bell (px)**		
	spectra	Average	min	max	Average	min	max	Average	min	max
PSM-ol	10	23	19	38	5	4	8	8	7	14
PSM-opx	6	1043	762	1264	186	144	218	201	147	243
PSM-cpx	6	997	711	1506	286	226	377	422	301	637
PSD#4-ol	9	328	265	383	59	48	76	117	95	137
PSD#4-opx	13	2952	2376	4433	499	445	735	568	457	853
PSD#4-cpx	15	3242	2925	3103	824	607	938	1372	1238	1313
PSD#5-ol	15	352	311	364	63	48	74	126	111	130
PSD#5-opx	11	3226	2905	3328	548	495	570	620	559	640
PSD#5-cpx	11	2666	2357	2655	700	567	797	1128	997	1123
PSD#6-ol	10	285	253	610	50	43	104	102	90	218
PSD#6-opx	5	3723	2878	4831	615	490	771	716	553	929
PSD#6-cpx	5	2698	2625	2514	695	626	727	1142	1111	1064

§ Number of spectra used for calculation of the average spectrum for each mineral phase, it is the same number for unpolarized and polarized spectra.
*NIA: normalized integrated absorbance from normalized and averaged spectra.
**Since the average of unpolarized and polarized spectra are not different, we have averaged all of them to calculate a 'master' average spectrum, which is used afterwards for estimation of the hydrogen concentrations and estimation of partition coefficients.

785
786
787
788
789
790
791
792
793
794

795
796 **Table 3.** Hydrogen concentration ratios from this study and partition coefficients from previous
797 experimentals studies as well as concentration ratios in mantle-derived peridotites. Partition coefficient are
798 compiled only for experimental runs where at least three NAMs are co-existing (ol+opx+cpx or
799 ol+opx+cpx+gt). Most of the previous studies used mostly used SIMS measurements, or FTIR or ERDA
800 or a combinaison of theses analytical methods to quantify hydrogen concentration.
801

Concentration ratio$	Ropx/ol	Rcpx/ol	Rcpx/opx	Remarks
PSM-0h	24.4	51.3	2.1	This study*, mantle xenolith
PSM4-10h	4.8	11.7	2.4	This study*, subsolidus, 3 GPa, 1100°C
PSM5-25h	4.9	8.9	1.8	This study*, subsolidus, 3 GPa, 1100°C
PSM6-110h	7.0	11.2	1.6	This study*, subsolidus, 3 GPa, 1100°C
Average	5.6	10.6	1.9	This study*, subsolidus, 3 GPa, 1100°C
Reference	Dopx/ol	Dcpx/ol	Dcpx/opx	
Hirth and Kohlstedt, 1996	5	10	2	with melt, constante values over P and T
Aubaud et al., 2004	9.1	12.5	1.4± 0.3	with melt, 1-2 GPa, 1230-1380 °C
Hauri et al., 2006** Tenner	12.2	14.6	1.2	with melt, 1.2-1.6 GPa, 1185-1370 °
et al., 2009# Kovàcs et al.,	n.d.	33	n.d.	C with melt, 3 GPa, 1450 °C
2012 Karimova and Stalder	4.7±1.1	16.45	3.5±1.5	with melt, 4 GPa, 1100-1225 °C
2013§ Novella et al., 2014 $	n.d.	n.d.	2.0±0.3	melt-free, 6 GPa, 1150-1300 °
	1.8	3.3	1.8	C with melt, 6 GPa, 1400 °C
Bell and Rossmann, 1992	62	176	2.8	Sp-lherzolite xenolith (KBH-1)
Bell and Rossmann, 1992	18	37	2.05	Gt-lherzolite xenolith (KOH-29) Gt-
Grant et al., 2007§	6.6	12.7	1.9	peridotite xenolith (South Africa)
SD&NBC, 2006	33	64	2.0	Date compil. / Sp- and Gt peridotite
St.Dev on SD&NBC, 2006	36	70	0.7	Date compil. / Sp- and Gt peridotite
Linear Fit, y=(a±a')x, a±a'=	11±1	21±5	1.9±0.1	Date compil. / Sp- and Gt peridotite
R^2 of the linear fit	0.17	0.06	0.82	Date compil. / Sp- and Gt peridotite

N.B.: Grant et al, 2006 and 2007b were excluded since the system is Fe-Al-free. Koga et al., (2003) and Férot and Bolfan-Casanova (2012) were excluded since no cpx were present in the run products.*The ratios are calculated using values obtained using Withers et al., (2012) and Bell et al., (1995) for olivine and pyroxenes respectively.** Only values from run B359, B366, B394 and B432 (at least ol+opx+cpx+melt) were taken into account for calculating an average reported here. # only 1 run M373 (assemblage ol+opx+cpx+melt) but opx could not be analysed in this run. $ only S5281 (assemblage ol+opx+cpx+gt+melt). § only KBJ30 and LMA 15, values were then averaged and reported here, values using the Libowitky and Rossman (1997) calibration were taken for olivine as it is closer to calibration of Withers et al., (2012). SD&NBC: Demouchy and Bolfan-Casanova, 2016. § based on runs AK019 and AK021 only, and following the calibration (Bell et al., 1995, 2004). $ The hydrogen concentrations ratios, calculated using other IR calibrations (B/B=Bell1995/Bell2003, P/P: Paterson1982/Paterson1982) yield: $D^{B/B}_{opx/ol=}$ 3.5 ; $D^{B/B}_{cpx/ol=}$ 6.7 ; $D^{P/P}_{opx/ol=}$ 9.7; $D^{P/P}_{cpx/ol=}$ 12.9 ; $D^{P/P}_{cpx/opx=}$ 12.9.

This is a preprint, the final version is subject to change, of the American Mineralogist (MSA)
Cite as Authors (Year) Title. American Mineralogist, in press.
(DOI will not work until issue is live.) DOI: http://dx.doi.org/10.2138/am-2017-6089

Demouchy et al., Figure 1R

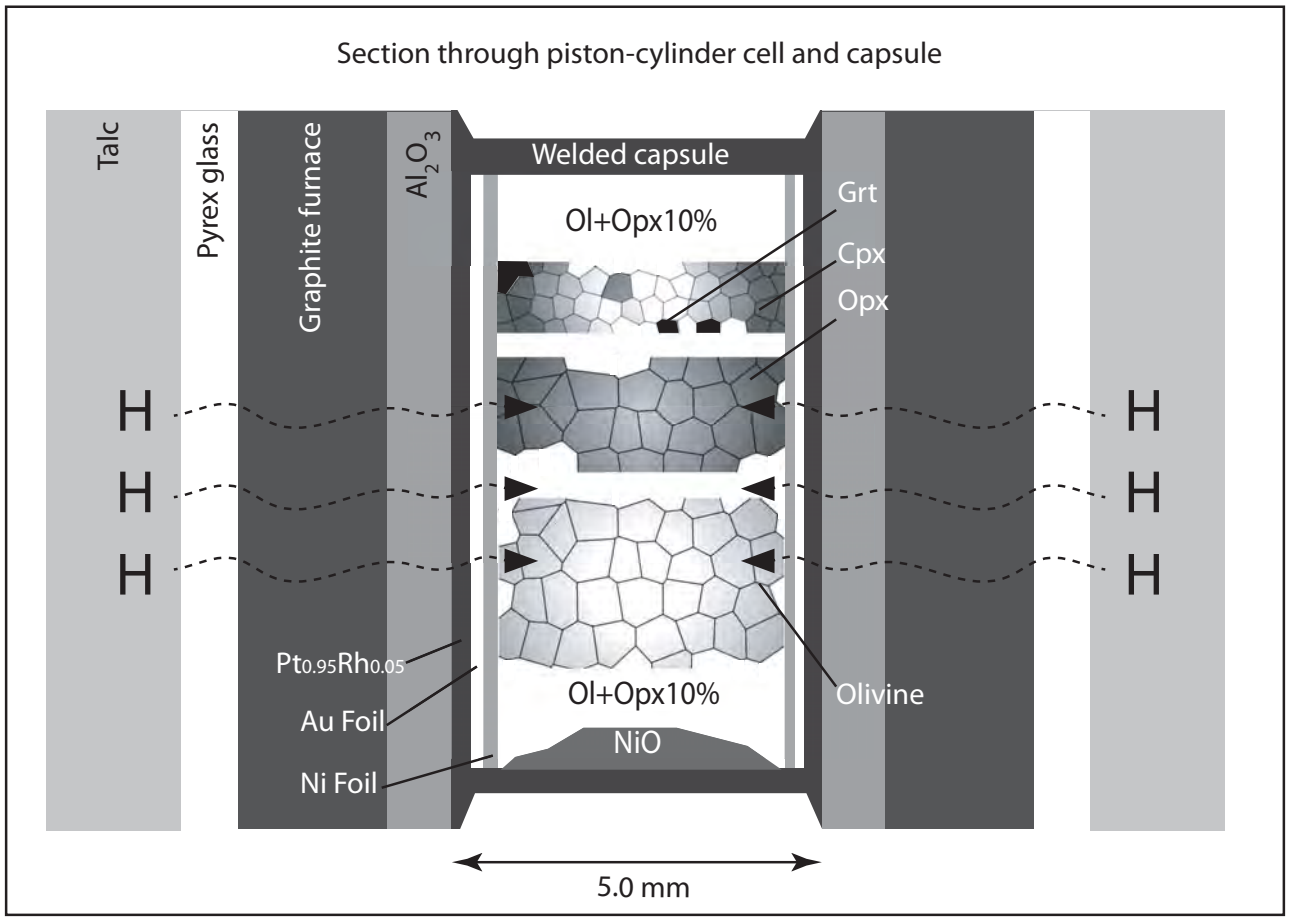

This is a preprint, the final version is subject to change, of the American Mineralogist (MSA)
Cite as Authors (Year) Title. American Mineralogist, in press.
(DOI will not work until issue is live.) DOI: http://dx.doi.org/10.2138/am-2017-6089

Demouchy et al., Figure 2

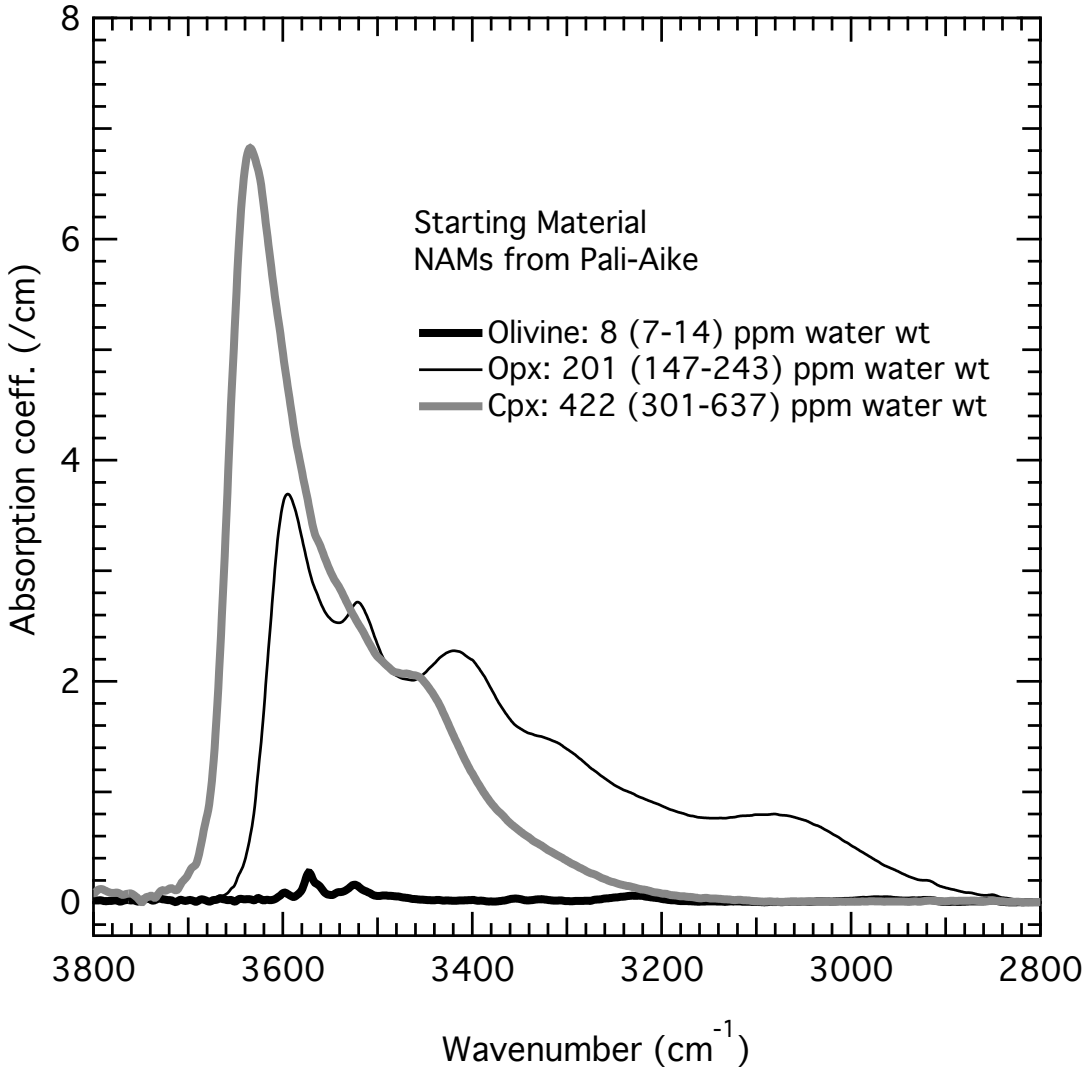

This is a preprint, the final version is subject to change, of the American Mineralogist (MSA)
Cite as Authors (Year) Title. American Mineralogist, in press.
(DOI will not work until issue is live.) DOI: http://dx.doi.org/10.2138/am-2017-6089

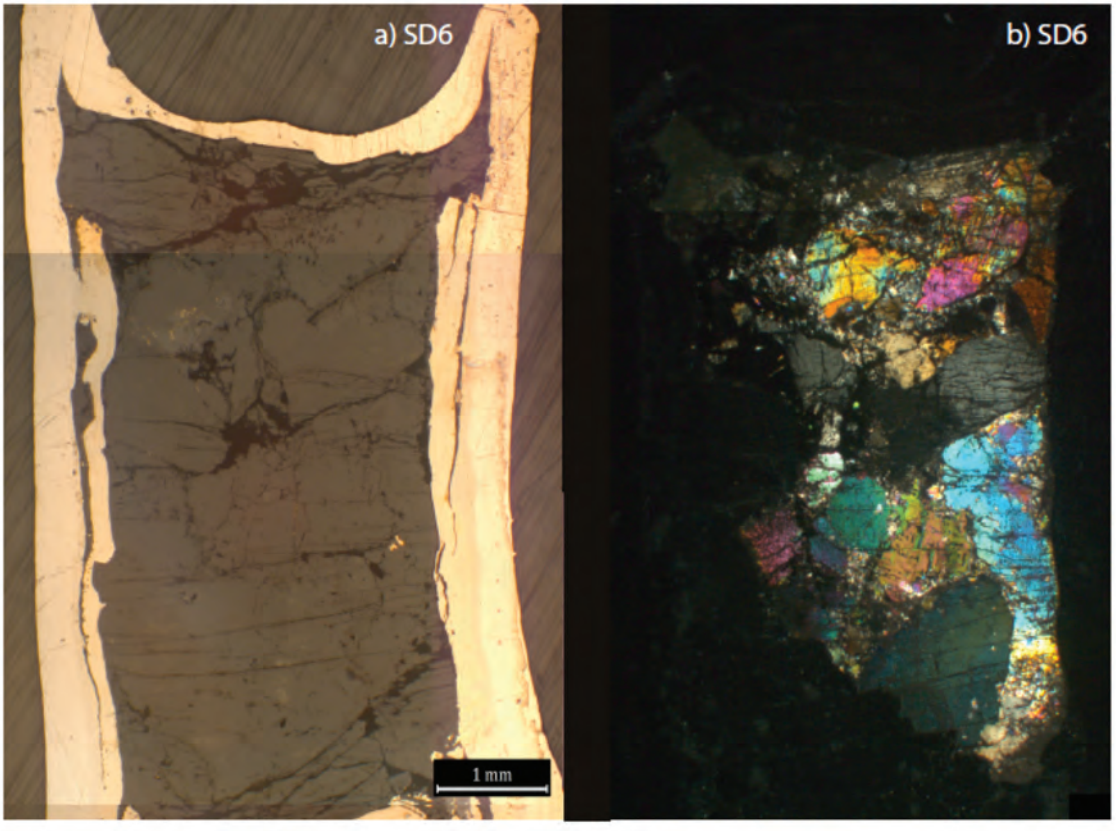

This is a preprint, the final version is subject to change, of the American Mineralogist (MSA)
Cite as Authors (Year) Title. American Mineralogist, in press.
(DOI will not work until issue is live.) DOI: http://dx.doi.org/10.2138/am-2017-6089

Demouchy et al., Fig. 4

a)

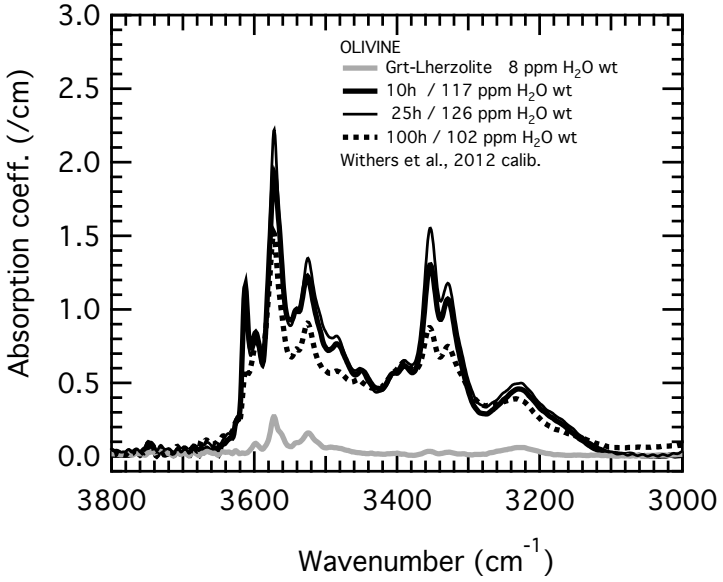

b)

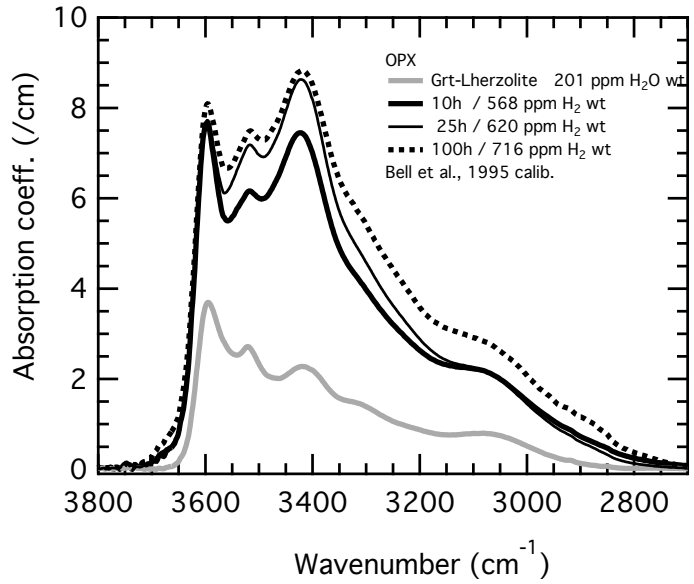

c)

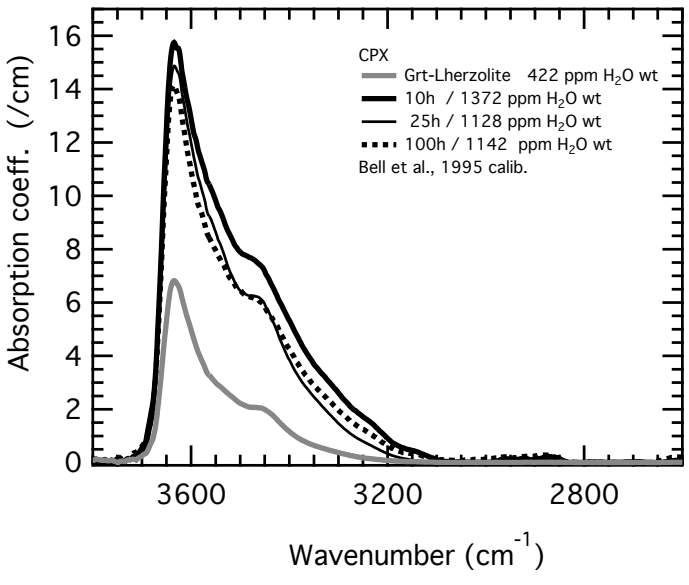

This is a preprint, the final version is subject to change, of the American Mineralogist (MSA)
Cite as Authors (Year) Title. American Mineralogist, in press.
(DOI will not work until issue is live.) DOI: http://dx.doi.org/10.2138/am-2017-6089

Demouchy et al., Figure 5

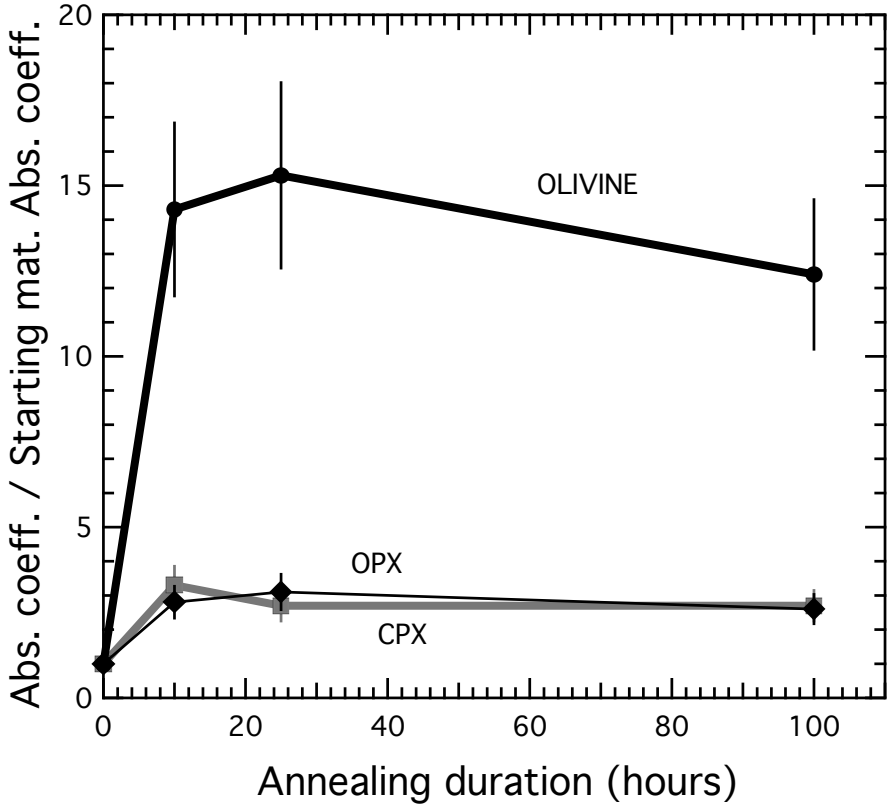

This is a preprint, the final version is subject to change, of the American Mineralogist (MSA)
Cite as Authors (Year) Title. American Mineralogist, in press.
(DOI will not work until issue is live.) DOI: http://dx.doi.org/10.2138/am-2017-6089

Demouchy et al., Figure 6